

# **The Effect of Annealing Atmospheres on Structural and Magnetic Properties of Mn-doped $\beta$ -Ga<sub>2</sub>O<sub>3</sub>**

Xu Dai, Xi Zhang, Gang Xiang\*

College of Physics, Sichuan University, Chengdu 610000, China.

\*Corresponding email: gxiang@scu.edu.cn

**Abstract:** Mn-doped  $\beta$ -Ga<sub>2</sub>O<sub>3</sub> (GMO) films with room-temperature ferromagnetism are synthesized on *c*-plane sapphire substrates by polymer-assisted deposition and the effects of annealing atmospheres (air and pure O<sub>2</sub> gas) on their structures and physical properties are investigated. The characterizations reveal that the concentrations of oxygen vacancies (V<sub>Os</sub>) and various Mn (Mn<sup>2+</sup>, Mn<sup>3+</sup> and Mn<sup>4+</sup>) ions in the GMO films are modulated by the annealing atmospheres. The inter-planar spacing of the samples annealed in air (GMO-air) with more Mn<sup>2+</sup> ions is larger than that of the samples annealed in pure O<sub>2</sub> gas (GMO-O<sub>2</sub>) with more Mn<sup>4+</sup> ions. Notably, GMO-air exhibits a saturation magnetization value as strong as 1.7 times that of GMO-O<sub>2</sub>, owing to the enhanced coupling between V<sub>Os</sub> and Mn ions as well as the spin polarization contribution from more 3*d* electrons in GMO-air. Besides, the optical properties and electrical resistivity of the GMO films are also tuned by the annealing atmospheres. Our results reveal the important effect of annealing atmospheres on the structural and magnetic properties of the GMO films and provide an alternative way for spintronic engineering of related materials.

**Key words:** Mn-doped  $\beta$ -Ga<sub>2</sub>O<sub>3</sub>; Annealing atmosphere; Oxygen vacancies; Ferromagnetism

## Introduction

Owing to the co-existence of charge and spin degrees of freedom in the diluted magnetic semiconductors (DMSs), tremendous attention has been aroused in semiconductor spintronics.[1-4] As a promising wide-bandgap material for various applications including solar-blind detectors and high-frequency power devices, gallium oxide ( $\text{Ga}_2\text{O}_3$ ) has attracted interest for its potentials in spintronic applications very recently.[5-7] It is found that, besides a weak long-distance ferromagnetism induced by coupling of gallium vacancies in undoped  $\text{Ga}_2\text{O}_3$ ,[8] the ferromagnetism in  $\text{Ga}_2\text{O}_3$  can be realized by doping with various metallic elements, such as Fe[9], Ni[10], Cr[11], Sn[12] and Mn[13-18]. For instance, Ni-doped  $\beta\text{-Ga}_2\text{O}_3$  nanoparticles with room-temperature ferromagnetism (RTFM) were synthesized by hydrothermal method, in which the ferromagnetism mainly came from the interaction between  $\text{Ni}^{2+}$  and  $\text{O}^{2-}$  ions and related defect contributions.[9] Peng *et al.* reported the coexistence of ferromagnetic and antiferromagnetic phases in the Mn-doped  $\beta\text{-Ga}_2\text{O}_3$  prepared by ion implantation.[13] Pei *et al.* reported the RTFM of Mn-doped  $\text{Ga}_2\text{O}_3$  and explained it using a carrier-mediated double exchange model.[14] Guo *et al.* found that both coercive field ( $H_C$ ) and saturation magnetization ( $M_s$ ) in Mn-doped  $\beta\text{-Ga}_2\text{O}_3$  increased with Mn doping concentration, which could be explained by coupling between Mn ions and oxygen vacancies ( $\text{V}_{\text{O}}$ ).[15] Huang *et al.* found that both Mn dopants and defects could affect the RTFM in Mn-doped  $\beta\text{-Ga}_2\text{O}_3$ . [16] On the other hand, the calculations based on density functional theory (DFT) suggested that the RTFM of Mn-doped  $\beta\text{-Ga}_2\text{O}_3$  came from the strong  $p$ - $d$  coupling and the delocalization of O-2p

orbitals.[17] Obviously, although much work has been done on the fabrication and characterization of ferromagnetic  $\text{Ga}_2\text{O}_3$ , the mechanism underlying the ferromagnetism still remains controversial, especially the role of oxygen in the ferromagnetic ordering in  $\text{Ga}_2\text{O}_3$ . Therefore, for both basic science and potential applications, it is important and necessary to further investigate the roles of oxygen and other structural factors on the ferromagnetism of  $\text{Ga}_2\text{O}_3$ .

In this work, Mn-doped  $\beta\text{-Ga}_2\text{O}_3$  (GMO) pre-films are first prepared by polymer assisted deposition (PAD) and then annealed in different atmospheres (air and pure  $\text{O}_2$  gas) to obtain GMO films with different concentrations of  $\text{V}_{\text{Os}}$  and various Mn ions. The structures of the GMO films are characterized and the effects of annealing atmospheres on the optical, electrical, and ferromagnetic properties of the films are then investigated.

## Experimental

The polyethyleneimine (PEI) ((M.W. 10,000, 99%, Sigma-Aldrich) and Ethylene Diamine Tetraacetic Acid (EDTA) (99.9%, Sigma-Aldrich) are added to deionized water in a certain proportion to prepare the polymer solution. Subsequently, gallium nitrate hydrate ( $\text{GaN}_3\text{O}_9 \cdot x\text{H}_2\text{O}$ , 99.9%, Sigma-Aldrich) is added to the polymer solution to obtain the Ga-polymers solution, and manganese chloride tetrahydrate ( $\text{MnCl}_2 \cdot 4\text{H}_2\text{O}$ , 99.9%, Sigma-Aldrich) is added to the polymer solution to obtain the Mn-polymers solution. The Mn-doped Ga precursor (GaMn-polymers) solution is prepared by adding the Mn-polymers solution to the Ga-polymers solution, which is then dropped on single crystalline *c*-plane

sapphire substrate to prepare pre-films using 30s-spin-coating at 3000 rpm. The GaMn-polymers are tested by thermalgravimetric analysis and differential scanning calorimeter (TGA-DSC) (TA instruments, Q40) in air and pure O<sub>2</sub> gas to study the changes of weight and calorie during annealing. Fig. 1(a) shows the TG and DSC curves of the GaMn-polymers in air. The exothermic peaks at 290°C and 484°C represent the decompositions of the GaMn-polymers, and the endothermic peak at 588°C represents the crystallization of Mn-doped gallium oxide. The TG and DSC curves in pure O<sub>2</sub> gas show similar results. Based on the TG-DSC results, the pre-films are heated up to 550 °C for 1 h to completely decompose PEI and EDTA, and then annealed at 750°C to obtain GMO-air and GMO-O<sub>2</sub> films in air and pure O<sub>2</sub> gas, respectively. The inset is the digital images of typical 2cm×2cm GMO-air and GMO-O<sub>2</sub> films, which show that the GMO films are translucent brown. By changing the concentration of the precursor solution and the number of suspension coatings, dozens to hundreds of nanometer-thick GMO films are obtained. For comparison, undoped β-Ga<sub>2</sub>O<sub>3</sub> films are also prepared.

Surface morphologies of the GMO films are depicted by atomic force microscope (AFM, Benyuan, CSPM5500). X-ray diffraction (XRD, Bruker D8, Empyrean analytical diffractometer) using a Cu Kα radiation source along with high-resolution transmission electron microscopy (HRTEM, Tecnai F30, FEI) is used to characterize crystalline structure of the GMO films. Cross-section samples for HRTEM and Spherical aberration TEM (STEM) measurements are prepared by focus ion beam (FIB) milling procedure in a Helios system (Tescan, LYRA 3 XMU). Elemental composition and valence are examined by X-

ray photoelectron spectroscopy (XPS, Kratos AXIS Supra). The optical properties are evaluated using UV-visible spectrophotometer (PerkinElmer Lambda 950 UV-Vis-NIR) and Photoluminescence (PL, LS-45). Magnetic properties and resistivity of the films are measured by Superconducting Quantum Interference Devices (SQUID, Quantum Design, MPMS-XL-5) and four-probe resistivity tester (FPPRT, ST-2722), respectively.

## Results and Discussion

The three-dimensional AFM images indicate that the surface roughness of the GMO films is  $\sim 1.2$  nm, as shown in Fig. 1(b). The crystal structures of the obtained translucent large-scale films are studied by XRD. As shown in Fig. 1(c), three diffraction peaks belong to (-201), (-402), and (-603) groups of the  $\beta$ -Ga<sub>2</sub>O<sub>3</sub> are observed in all the samples, indicating the (-201) preferential growth orientation in the PAD films.[19] No peaks of Mn metal clusters, Mn oxides or compounds are found, which are consistent with the results of Mn-doped  $\beta$ -Ga<sub>2</sub>O<sub>3</sub> in the literature [15,16]. Only one crystallization peak in the DSC curve of the GaMn-polymers also indicates the single crystal phase during annealing, as shown in Fig. 1(a). As shown in Fig. 1(d), comparing with those of un-doped  $\beta$ -Ga<sub>2</sub>O<sub>3</sub>, the diffraction peaks of the GMO-air films are left-shifted, implying the increasing of inter-planar spacing, while the diffraction peaks of the GMO-O<sub>2</sub> films are marginally right-shifted. Based on the calculations using Bragg equation, the (-402) inter-planar spacings of un-doped  $\beta$ -Ga<sub>2</sub>O<sub>3</sub>, GMO-air and GMO-O<sub>2</sub> films, are obtained as 0.232 nm, 0.240 nm and 0.230 nm, respectively. Since the radii of the cations are as follows:  $\text{Mn}^{2+}$  (0.83 Å) >  $\text{Mn}^{3+}$

(0.64 Å) > Ga<sup>3+</sup> (0.62 Å) > Mn<sup>4+</sup> (0.53 Å), [15] different Mn ions replacing Ga<sup>3+</sup> ions in the Ga<sub>2</sub>O<sub>3</sub> lattice result in different inter-planar spacings. According to Fig. 1(d), more Mn<sup>2+</sup> ions are incorporated in GMO-air films, while more Mn<sup>4+</sup> ions are incorporated in GMO-O<sub>2</sub> films.

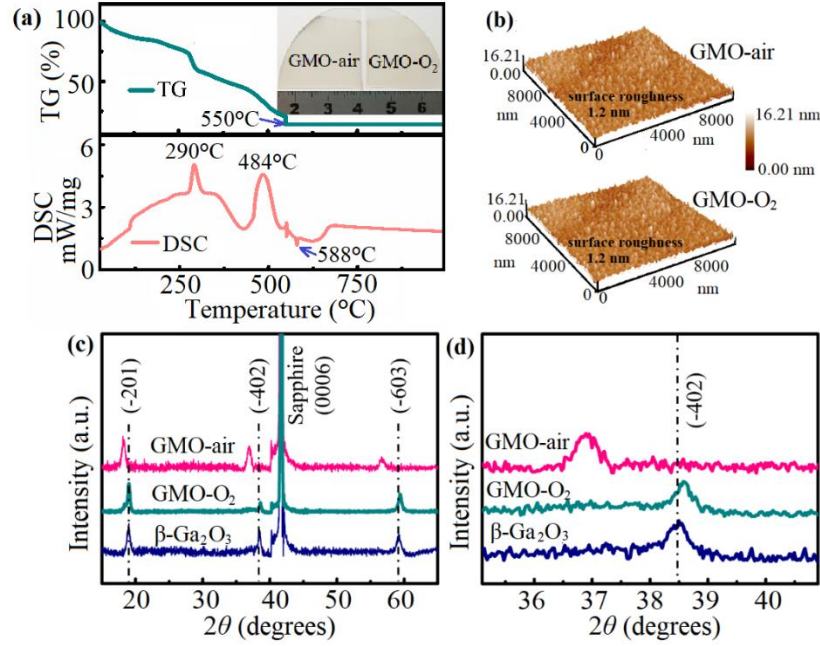
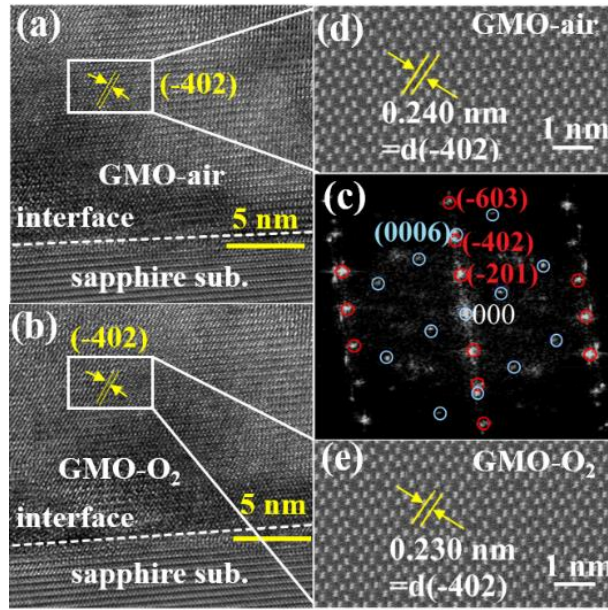


Fig. 1 (a) TG and DSC curves of the GaMn-polymers in the air. (b) 3D AFM images and digital photos of the GMO-air and GMO-O<sub>2</sub> films grown on the sapphire substrates. (c) XRD patterns of the PAD-grown GMO-air, GMO-O<sub>2</sub> and undoped β-Ga<sub>2</sub>O<sub>3</sub> films on the *c*-plane sapphire. (d) Enlarged view of  $\theta$ -2 $\theta$  XRD patterns around 38°.

The microstructures of the GMO films are then studied by TEM. HRTEM images of the GMO-air and GMO-O<sub>2</sub> films are shown in Fig. 2(a-b), respectively, which exhibit almost the same fast Fourier transformation (FFT). A typical FFT of GMO-air films is shown in Fig. 2(c). HRTEM and FFT images show that both GMO-air and GMO-O<sub>2</sub> films are highly

crystalline and grown along the direction of  $(-201)$ , consistent with the XRD results. STEM images of the GMO-air and GMO-O<sub>2</sub> films are shown in Fig. 2 (d-e), respectively. Clear crystalline structures can be seen and no Mn interstitials can be found in both cases. The inter-planar spacings along  $(-402)$  azimuth of the GMO-air and GMO-O<sub>2</sub> films are about 0.240 nm and 0.230 nm, respectively, consistent with the XRD results.



Fi. 2 Cross-sectional HRTEM images of (a) GMO-air and (b) GMO-O<sub>2</sub>. (c) FFT image of GMO-air. STEM images of (d) GMO-air and (e) GMO-O<sub>2</sub>.

To investigate the effect of annealing atmospheres on the chemical states of the elements, XPS measurements are performed on the GMO-air and GMO-O<sub>2</sub> films. The XPS spectra are collimated with C 1s characteristic peak. Fig. 3(a) and (b) show the O 1s spectra of the GMO-air and GMO-O<sub>2</sub> films, respectively. Each O 1s peak could be fitted into two sub-peaks, located at 530.7 eV and 532.1 eV, corresponding to lattice oxygen (O<sub>lat</sub>) and V<sub>O</sub>,

respectively.[20] The  $V_O$  concentrations of the GMO-air and GMO-O<sub>2</sub> films are estimated to be 30% and 18%, respectively. The Mn doping concentrations in the GMO-air and GMO-O<sub>2</sub> films both are about 34.5%, estimated by fitting the XPS whole scanning spectra (not shown). Fig. 3(c) and (d) show the Mn 2p spectra of the GMO-air and GMO-O<sub>2</sub> films, respectively. The main peak can be fitted into three sub-peaks located at 640.59 eV, 641.74 eV and 643.00 eV, corresponding to  $Mn^{2+}$ ,  $Mn^{3+}$  and  $Mn^{4+}$  ions, respectively. [15,21] The concentrations of  $Mn^{2+}$ ,  $Mn^{3+}$  and  $Mn^{4+}$  ions in the GMO-air films are obtained as 10.4%, 11.4% and 12.7%, respectively, while the concentrations of  $Mn^{2+}$ ,  $Mn^{3+}$  and  $Mn^{4+}$  ions in the GMO-O<sub>2</sub> films are 2.8%, 13.1% and 18.6%, respectively. The concentrations of  $V_O$ s and different Mn ions in the GMO films are shown in Fig. 3(e). Much more  $Mn^{2+}$  ions are observed in GMO-air films, which are responsible for the increase of inter-planar spacing shown in Fig. 1(d). Meanwhile, more  $Mn^{4+}$  ions are observed in GMO-O<sub>2</sub> films, which are responsible for the decrease of inter-planar spacing shown in Fig. 1(d). It is worthwhile noting that this is the first time that  $Mn^{4+}$  ions are observed in Mn-doped Ga<sub>2</sub>O<sub>3</sub>. The fact that GMO-O<sub>2</sub> films have more  $Mn^{4+}$  ions indicates that sufficient oxygen in the annealing atmospheres favors the  $Mn^{4+}$  ions formation. The formation of different Mn ions can be understood in terms of different chemical surroundings as follows. [17] The substitutional Mn elements exhibit +3 valence state ( $Mn^{3+}$ ) without  $V_O$ s and gallium vacancies ( $V_{Ga}$ s) nearby, exhibit +2 valence state ( $Mn^{2+}$ ) with  $V_O$ s nearby and provide extra electrons to *d*-shell, and exhibit +4 valence state ( $Mn^{4+}$ ) with  $V_{Ga}$ s nearby and provide holes, respectively, as shown in Fig. 3(f-h).

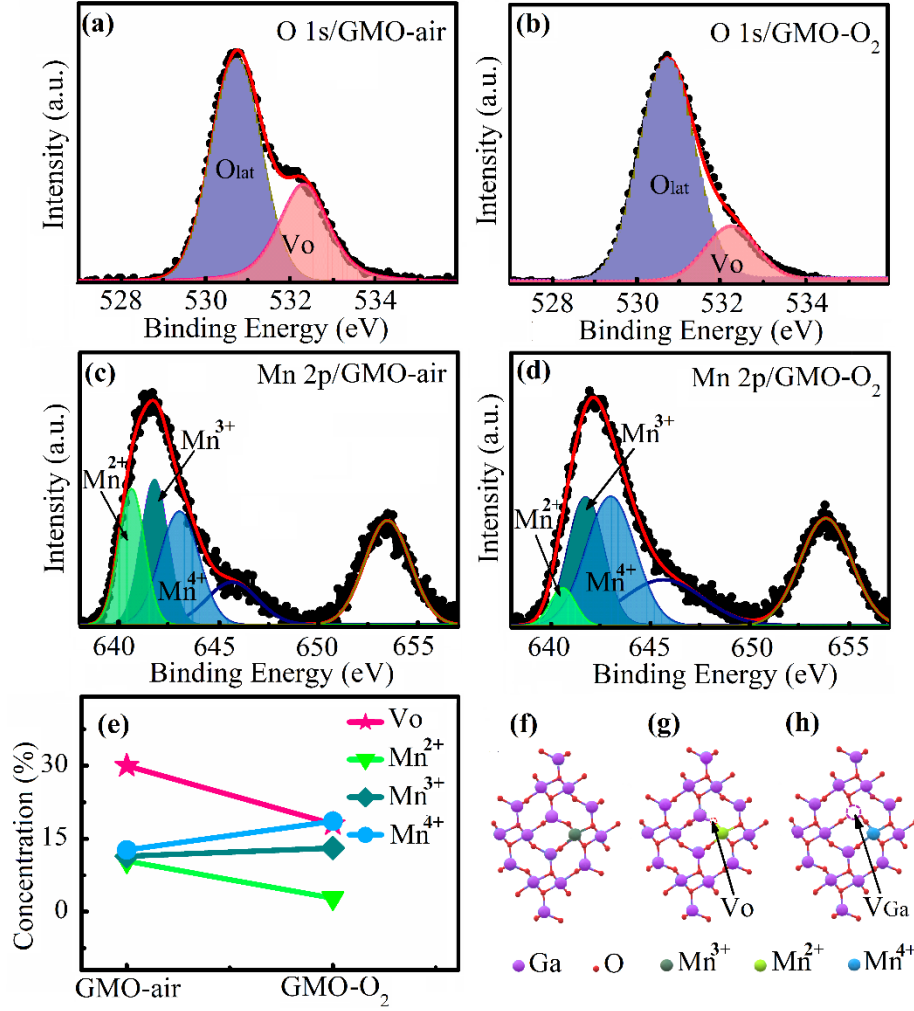


Fig. 3 O 1s peaks of (a) GMO-air and (b) GMO-O<sub>2</sub>. Mn 2p peaks of (c) GMO-air and (d) GMO-O<sub>2</sub>. (e) The concentrations of V<sub>o</sub>s and different Mn ions in the GMO films. The schematic diagram of formation of (f) Mn<sup>3+</sup>, (g) Mn<sup>2+</sup> and (h) Mn<sup>4+</sup> ions in the GMO films.

Fig. 4(a) shows the optical transmittance measured by a spectrophotometer of the GMO films. The GMO-air film exhibits slightly lower optical transmittance than that of the GMO-O<sub>2</sub> film, consistent with the results observed in Fig. 1(a). The inset is the  $(\alpha h\nu)^2$  versus  $h\nu$  plot of the GMO films. By fitting the plot of  $(\alpha h\nu)^2$  versus  $h\nu$ , the band gaps of

GMO-air and GMO-O<sub>2</sub> films are obtained as 4.98 eV and 5.18 eV, respectively. It is more V<sub>Os</sub> in GMO-air films that result in lower optical transmittance and smaller band gap, owing to the contributions of more occupied defect levels. [22,23] Fig. 4(b) shows the PL spectra of the GMO films measured at room temperature with an excitation wavelength of 250 nm. The emission band can be divided into four bands centered at about 345 nm, 415 nm, 440 nm and 480 nm, respectively. The ultraviolet emission band located at about 345 nm corresponds to the recombination of self-trapped excitons, which is an intrinsic process.[24] The emission peaks centered at 415 nm, 440 nm (violet region) and 480 nm (blue region) are originated from the electron-hole recombination formed by V<sub>Os</sub>, or from the recombination of Ga-O vacancy pair.[25,26] The PL intensity at the violet and blue regions of the GMO-air films are stronger than that of GMO-O<sub>2</sub> films, which can be attributed to more defects such as V<sub>Os</sub> in the GMO-air films. The electrical resistivity values of the GMO-air and GMO-O<sub>2</sub> films are measured by four-probe resistivity tester and obtained as  $1.2 \times 10^4 \text{ } \Omega \cdot \text{cm}$  and  $9.1 \times 10^4 \text{ } \Omega \cdot \text{cm}$ , respectively, which can be roughly explained by the fact that more V<sub>Os</sub> exist in GMO-air films since V<sub>Os</sub> act as donor-type defects to provide electrons in Ga<sub>2</sub>O<sub>3</sub>. In short, the large difference between the V<sub>O</sub> concentrations in the GMO-air and GMO-O<sub>2</sub> films results in the tuning of the optical and electrical properties.

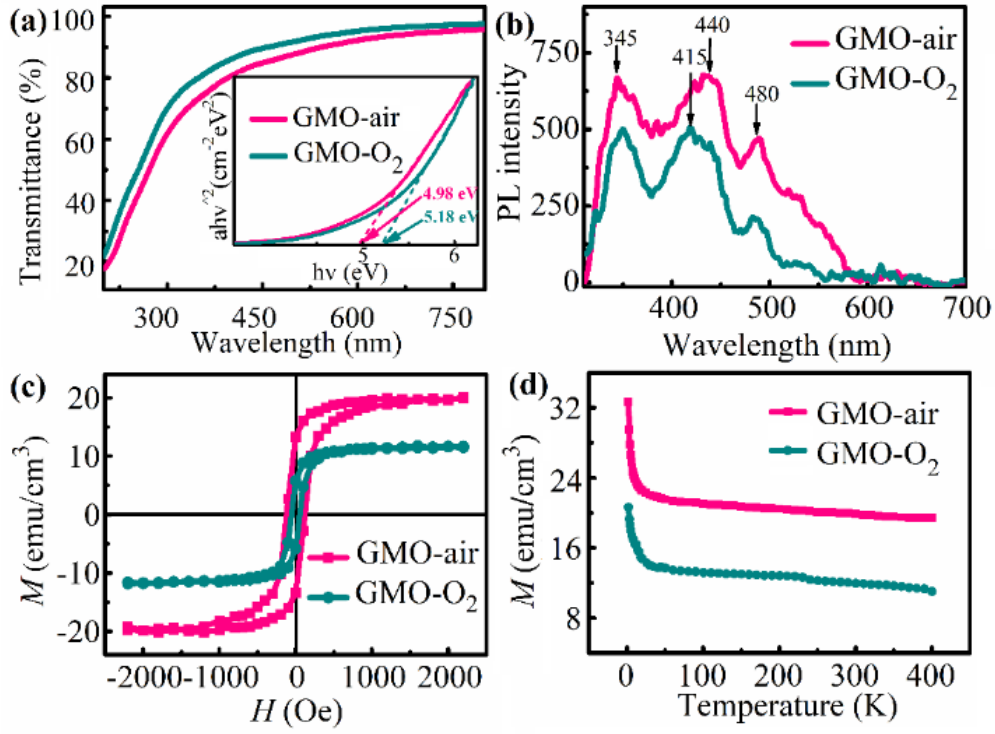


Fig. 4 (a) Optical transmittance spectra of the GMO films. Inset is the  $(\alpha h\nu)^2$  versus  $h\nu$  plot of the GMO films. (b) Room-temperature PL spectra of the GMO films excited at 250 nm. (c) M-H curves of the GMO films at 300 K. (d) Temperature-dependent magnetization of the GMO films.

Fig. 4(c) shows the magnetization versus magnetic field ( $M$ - $H$ ) curves of the GMO films obtained at 300 K, in which  $H$  is swept in plane since the easy magnetic axis of the films is in-plane.[16] Both GMO films display typical hysteresis loops, which are clear signals of ferromagnetism. The  $M_S$  values of the GMO-air and GMO-O<sub>2</sub> films are 19.7 emu/cm<sup>3</sup> and 11.6 emu/cm<sup>3</sup>, corresponding to magnetic moments of 0.09  $\mu_B$ /Mn and 0.05  $\mu_B$ /Mn, respectively. The  $H_C$  values of the GMO-air and GMO-O<sub>2</sub> films are 120 Oe and 58 Oe,

respectively. Obviously, GMO-air exhibits stronger  $M_S$  and  $H_C$  values, 1.8 and 2.1 times those of GMO-O<sub>2</sub>, respectively. The temperature-dependent magnetization ( $M$ - $T$ ) curves of the GMO-air and GMO-O<sub>2</sub> films measured in field-cooling mode under 2000 Oe are shown in Fig. 4(d), which are clearly indicative of ferromagnetism up to temperatures higher than 400 K. The magnetizations of both samples increase very slowly from 400 K down to 20 K, and then increase steeply at temperatures lower than 20 K, which is also observed in Mn-doped  $\gamma$ -Ga<sub>2</sub>O<sub>3</sub> and ascribe to the presence of paramagnetic components inducing additional magnetization at low temperatures.[18] Notably, the  $M$ - $T$  curves also reveal stronger magnetization in GMO-air films.

The discrepancy in the magnetic parameters between the GMO-air and GMO-O<sub>2</sub> films with the same Mn doping level can be understood as follows. The greater  $H_C$  value in the GMO-air films is ascribed to more V<sub>OS</sub>, since the  $H_C$  value increases with the increase of pinning sites originated from the V<sub>OS</sub> in oxide films.[27] The enhancement of the  $M_S$  value in the GMO-air films can be explained by the bound magnetic polaron (BMP) model as well as the spintronic contribution from the Mn<sup>2+</sup> ions. [15,28] In comparison with GMO-O<sub>2</sub>, more V<sub>OS</sub> are induced and more BMPs are thus established via coupling between V<sub>OS</sub> and Mn ions in GMO-air, resulting in stronger magnetization. In addition, GMO-air has more Mn<sup>2+</sup> ions than GMO-O<sub>2</sub>, which can provide more 3d electrons for stronger spin polarization than Mn<sup>3+</sup> and Mn<sup>4+</sup> ions. As a result, the ferromagnetism in GMO-air is greatly enhanced. Therefore, it is the different annealing atmospheres that modulate the magnetizations in the GMO films by engineering the concentrations of V<sub>OS</sub> and various Mn

ions in different chemical valence states.

## Conclusions

The GMO films with RTFM are successfully prepared by PAD. By annealing the GMO films in different annealing atmospheres (air and pure O<sub>2</sub> gas), the concentrations of V<sub>OS</sub> and various Mn (Mn<sup>2+</sup>, Mn<sup>3+</sup> and Mn<sup>4+</sup>) ions and hence the coupling between V<sub>OS</sub> and Mn ions are modulated. Consequently, the optical, electrical, and ferromagnetic properties of the annealed GMO films are tuned. Our results provide insights into the role of the V<sub>O</sub> concentration as well as the chemical states of Mn elements in the ferromagnetism of β-Ga<sub>2</sub>O<sub>3</sub> and may be useful for related electronic and spintronic applications.

## References

- [1] S. Fusil, V. Garcia, A. Barthélémy, et al. Magnetoelectric Devices for Spintronics[J]. *Annu. Rev. Mater. Res.* , 2014, 44(1):91-116.
- [2] P. Dorpe, Z. Liu, W. Roy, et al. Very high spin polarization in GaAs by injection from a (Ga,Mn)As Zener diode, *Appl. Phys. Lett.* , 2004, 84: 3495-3497.
- [3] Z. Li, W. Bai, Y. Li, et al. Coexistence of large positive and negative magnetoresistance in Cr<sub>2</sub>Si<sub>2</sub>Te<sub>6</sub> ferromagnetic semiconductor. *Sci. China Mater.* , 2021, 65(3): 780-787.
- [4] Y. Liu, G. Wang, S. Wang, et al. Defect-Induced Magnetism in Neutron Irradiated 6H-SiC Single Crystals [J]. *Phys. Rev. Lett.* , 2011, 106: 087205.
- [5] W.Y. Kong, G. Wu, K. Wang, et al. Graphene-beta-Ga<sub>2</sub>O<sub>3</sub> Heterojunction for Highly

- Sensitive Deep UV Photodetector Application [J], *Adv. Mater.* , 2016, 28: 10725.
- [6] M. Higashiwaki, K. Sasaki, H. Murakami, et al. Recent progress in Ga<sub>2</sub>O<sub>3</sub> power devices [J], *Semicond. Sci. Tech.* , 2016, 31, 034001.
- [7] M. Passlack, M. Hong, J.P. Mannaerts, et al. Thermodynamic and photochemical stability of low interface state density Ga<sub>2</sub>O<sub>3</sub>-GaAs structures fabricated by in situ molecular beam epitaxy [J], *Appl. Phys. Lett.* , 1996, 69: 302.
- [8] Y. Yang, J. Zhang, S. Hu, et al. First-principles study of Ga-vacancy induced magnetism in  $\beta$ -Ga<sub>2</sub>O<sub>3</sub>, *Phys. Chem. Chem. Phys.* , 2017, 19: 28928–28935
- [9] Y. Huang, A. Gao, D. Guo, et al. Fe doping-stabilized  $\gamma$ -Ga<sub>2</sub>O<sub>3</sub> thin films with a high room temperature saturation magnetic moment[J]. *J. Mater. Chem. C*, 2020, 8: 536-542.
- [10] S. Ye, Y. Zhang, H. He, et al. Simultaneous broadband near-infrared emission and magnetic properties of single phase Ni<sup>2+</sup>-doped  $\beta$ -Ga<sub>2</sub>O<sub>3</sub> nanocrystals via mediated phase-controlled synthesis[J]. *J. Mater. Chem. C*, 2015, 3: 2886-2896.
- [11] D. Guo, Z. Wu, et al. Magnetic anisotropy and deep ultraviolet photoresponse characteristics in Ga<sub>2</sub>O<sub>3</sub>:Cr vermicular nanowire thin film nanostructure[J]. *Rsc. Adv.* , 2015, 5: 12894–12898.
- [12] E. Chikoidze, H. Bardeleben, K. Akaiwa, et al. Electrical, optical, and magnetic properties of Sn doped  $\beta$ -Ga<sub>2</sub>O<sub>3</sub> thin films[J]. *J. Appl. Phys.* , 2016, 120:025109.
- [13] B. Peng, Y. Zhang, Y. Wang, et al. Observation of room temperature ferromagnetism and exchange bias in a <sup>55</sup>Mn<sup>+</sup> ion-implanted unintentionally doped  $\beta$ -Ga<sub>2</sub>O<sub>3</sub> single

- crystal[J]. J. Magn. Magn. Mater. , 2020, 506: 166687.
- [14] G. Pei, C. Xia, Y. Dong, et al. Studies of magnetic interactions in Mn-doped  $\beta$ -Ga<sub>2</sub>O<sub>3</sub> from first-principles calculations[J]. Scripta Mater. , 2008, 58: 943.
- [15] D. Guo, Z. Wu, Y. An, et al. Room temperature ferromagnetism in (Ga<sub>1-x</sub>Mn<sub>x</sub>)<sub>2</sub>O<sub>3</sub> epitaxial thin films[J]. J. Mater. Chem. C, 2015, 3: 1830–1834.
- [16] Y. Huang, Z. Chen, X. Zhang, et al. The structure and magnetic properties of  $\beta$ -(Ga<sub>0.96</sub>Mn<sub>0.04</sub>)<sub>2</sub>O<sub>3</sub> thin film \*[J]. J. Semicond. , 2018, 39: 053002.
- [17] X. Wang, R. Quhe, Y. Zhi, et al. The electronic structure and magnetic property of the Mn doped  $\beta$ -Ga<sub>2</sub>O<sub>3</sub>[J]. Superlattice. Microst. , 2019, 125:330-337.
- [18] H. Hayashi, H. Rong, H. Ikeno, et al. Room temperature ferromagnetism in Mn-doped gamma-Ga<sub>2</sub>O<sub>3</sub> with spinel structure[J]. Appl. Phys. Lett. , 2006, 89(18):181903.
- [19] T. Oshima, T. Okuno and S. Fujita, et al. Ga<sub>2</sub>O<sub>3</sub> Thin Film Growth on c-Plane Sapphire Substrates by Molecular Beam Epitaxy for Deep-Ultraviolet Photodetectors [J], Jpn. J. Appl. Phys. ,2007, 46 (11): 7217-7220.
- [20] X. Dai, Q. Zheng, X. Zhang, et al. High performance photoresponse of transparent  $\beta$ -Ga<sub>2</sub>O<sub>3</sub> film prepared by polymer-assisted deposition[J]. Mater. Lett. , 2021, 284(1):1-4.
- [21] D. Guo, P. Li , Z. Wu, et al. Inhibition of unintentional extra carriers by Mn valence change for high insulating devices[J]. Sci. Rep-UK, 2016, 6: 24190.
- [22] H. Liu, F. Zeng, Y. Lin, et al. Correlation of oxygen vacancy variations to band gap changes in epitaxial ZnO thin films[J]. Appl. Phys. Lett. , 2013, 102(18):041301.

- [23] Q. Zhou, X. Tao, G. Di, et al. SO<sub>2</sub> Tolerance and Mechanism of Elemental Mercury Removal from Flue Gas by a Magnetic Recyclable Fe<sub>6</sub>Mn<sub>0.8</sub>Ce<sub>0.2</sub>O<sub>y</sub> Sorbent[J]. *Energ. Fuel.* , 2021, 35(6): 5101-5109.
- [24] S. Rafique, L. Han, H. Zhao, et al. Thermal annealing effect on  $\beta$ -Ga<sub>2</sub>O<sub>3</sub> thin film solar blind photodetector heteroepitaxially grown on sapphire substrate[J]. *Phys. Status Solidi A*, 2017, 214(8): 1700063.1-1700063.6.
- [25] L. Binet, D. Gourier, et al. Origin of the blue luminescence of  $\beta$ -Ga<sub>2</sub>O<sub>3</sub>. *J. Phys. Chem. Solids*, 1998, 59: 1241–1249.
- [26] K. W. Chang, J. J. Wu, et al. Low-Temperature Growth of Well-Aligned  $\beta$ -Ga<sub>2</sub>O<sub>3</sub> Nanowires from a Single-Source Organometallic Precursor. *Adv. Mater.* , 2004, 16: 545–549.
- [27] J. Zhou, H. He, C. Nan, et al. Effects of substrate temperature and oxygen pressure on the magnetic properties and structures of CoFe<sub>2</sub>O<sub>4</sub> thin films prepared by pulsed laser deposition, *Appl. Surf. Sci.* 2007, 253: 7456–7460.
- [28] Y. Huang, A. Gao, D. Guo, et al. Fe doping-stabilized  $\gamma$ -Ga<sub>2</sub>O<sub>3</sub> thin films with a high room temperature saturation magnetic moment[J]. *J. Mater. Chem. C*, 2020, 8(2): 536-542.